ADVANCED FUNCTIONAL MATERIALS
www.afm-journal.de

Colloidal Bi_2S_3 Nanocrystals: Quantum Size Effects and Midgap States

Mauro Aresti, Michele Saba, Roberto Piras, Daniela Marongiu, Guido Mula, Francesco Quochi, Andrea Mura, Carla Cannas, Mauro Mureddu, Andrea Ardu, Guido Ennas, Vasco Calzia, Alessandro Mattoni, Anna Musinu, and Giovanni Bongiovanni**

Among solution-processed nanocrystals containing environmentally benign elements, bismuth sulfide (Bi_2S_3) is a very promising n-type semiconductor for solar energy conversion. Despite the prompt success in the fabrication of optoelectronic devices deploying Bi_2S_3 nanocrystals, the limited understanding of electronic properties represents a hurdle for further materials developments. Here, two key materials science issues for light-energy conversion are addressed: bandgap tunability via the quantum size effect, and photocarrier trapping. Nanocrystals are synthesized with controlled sizes varying from 3 to 30 nm. In this size range, bandgap tunability is found to be very small, a few tens of meV. First principles calculations show that a useful blueshift, in the range of hundreds of meV, is achieved in ultra-small nanocrystals, below 1.5 nm in size. Similar conclusions are envisaged for the class of pnictide chalcogenides with a ribbon-like structure $[Pn_4Ch_6]_n$ (Pn = Bi, Sb; Ch = S, Se). Time-resolved differential transmission spectroscopy demonstrates that only photoexcited holes are quickly captured by intragap states. Photoexcitation dynamics are consistent with the scenario emerging in other metal–chalcogenide nanocrystals: traps are created in metal-rich nanocrystal surfaces by incomplete passivation by long fatty acid ligands. In large nanocrystals, a lower bound to surface trap density of one trap every sixteen Bi_2S_3 units is found.

1. Introduction

Colloidal semiconductor nanocrystals are promising materials for applications in solution-processable optoelectronic devices including light-emitting diodes, photodetectors, photocatalysts and photovoltaic cells.[1–5] Chemical synthesis enables refined control over dimension and shape of nanocrystals, allowing for unique functionalities and novel physical properties.[6] A wide variety of materials has been used to fabricate semiconductor nanocrystals, but most of them employs materials containing heavy metal elements as cations, such as Pb or Cd, which could pose health hazard if deployed on large scale. For this reason, environmentally benign nanocrystals are currently a very central topic in materials research for solar energy conversion.[7–13]

Bismuth sulfide (Bi_2S_3) belongs to the class of non-toxic semiconductor materials that can be synthesized in nanocrystalline form by cheap colloidal synthesis.[14] The large absorption cross-section and the direct band gap in the near infrared have further attracted significant interest.[15] So far, research efforts have been addressed to the fabrication of solution-processed optoelectronic devices, including high-efficiency Vis-NIR photodetectors,[16] inorganic[7] and hybrid[8,9,17] bulk nano-heterojunctions for solar energy conversion and sensitized mesoscopic solar cells.[18] Several synthesis approaches have been also proposed to improve the control of nanocrystal size and shape.[14,15,17,19–25]

This growing attention has not seen a parallel progress in understanding some key physical materials properties. Band gap tunability via the quantum size effect is a nanocrystal property that can be exploited to develop unique photovoltaic cell architectures for a more efficient solar light conversion.[6,26–28] Nonetheless, the question concerning the extent to which the optical band gap can be tuned in Bi_2S_3 nanocrystals has not yet received an adequate quantitative answer.[15,25] Only recently, theoretical investigations have started addressing this issue in the framework of atomistic simulations,[29] but a systematic experimental-theoretical

M. Aresti, Dr. M. Saba, R. Piras, Dr. D. Marongiu, Dr. Guido Mula, Dr. F. Quochi, Prof. A. Mura, V. Calzia, Prof. G. Bongiovanni
Dipartimento di Fisica
Università degli Studi di Cagliari
Cittadella Universitaria
S.P. Monserrato-Sestu km 0.7
I-09042, Monserrato, Italy
E-mail: giovanni.bongiovanni@dsf.unica.it
Dr. C. Cannas, Dr. M. Mureddu, Dr. A. Ardu, Prof. Guido Ennas, Prof. A. Musinu
Dipartimento di Scienze Chimiche e Geologiche
Università degli Studi di Cagliari
Cittadella Universitaria
S.P. Monserrato-Sestu km 0.7
I-09042, Monserrato, Italy
E-mail: musinu@unica.it
V. Calzia, Dr. A. Mattoni
CNR-IOM Cagliari
Cittadella Universitaria
I-09042, Monserrato, (Ca), Italy

DOI: 10.1002/adfm.201303879

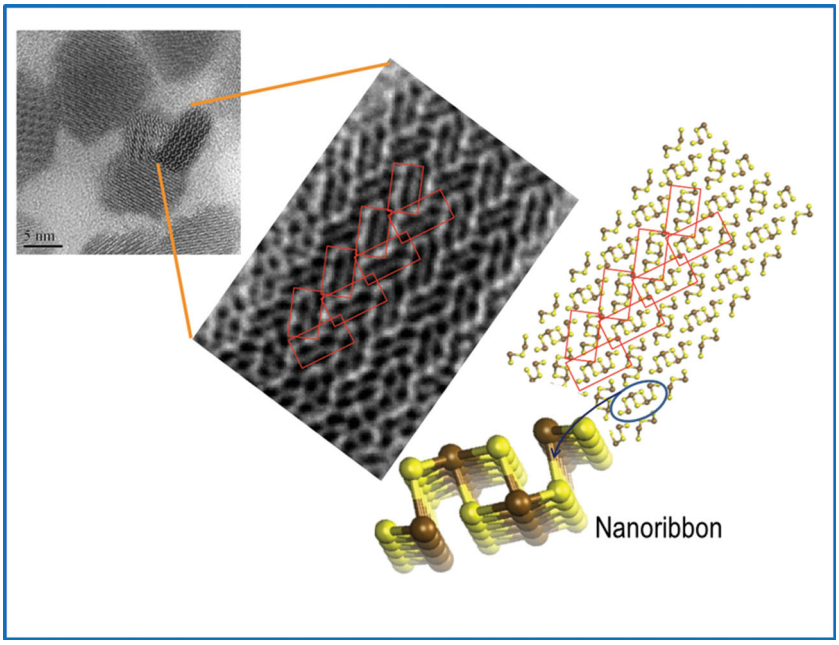

Figure 1. High-resolution transmission electron microscopy (HR-TEM) image of Bi_2S_3 nanocrystals. The orthorhombic crystal structure is formed by the assembling of atomic ribbons. In the nanocrystal shown in the enlarged image, the nanoribbon axis is along the [001] crystallographic direction and perpendicular to the figure plane. Ribbons are arranged in a herring-bone motif, as highlighted by the red rectangles.

comparison is still missing. A distinguishing property of Bi_2S_3 is the strong anisotropic crystal structure, consisting of weakly interacting one-dimensional ribbons, made by tightly-bonded $[Bi_4S_6]$ units in an herring-bone arrangement (see **Figure 1**).[30] Until now, the importance of this singular crystal structure for the band gap tunability and surface properties of nanocrystals has been neglected.

A deep knowledge of electron and hole recombination mechanisms at play in colloidal nanocrystals is also of crucial importance for successful exploitation of these materials in optoelectronic devices.[6] Photoexcited electrons and holes can quickly relax to the lowest and highest quantized levels of the conduction and valence bands, respectively. However, photocarriers can be also captured by intragap trap levels, whose contribution to charge transport is quite limited.[26,31] Engineering of surface traps to control recombination rate is critical for the design of sensitive and fast photoconductive detectors, while suppression of nonradiative recombinations and charge trapping is of paramount importance in solar cells.[2,3,32] There exists an extensive literature in semiconductor nanocrystals dedicated to the investigation of the relaxation dynamics of photoexcitations, to reveal the presence of carrier trap states, their energy and characteristic lifetimes, and their connection with surface properties.[6,31,33–39] Apart from an early report in Bi_2S_3 nanocrystals with band gap at 1.7 eV,[40] to the best of our knowledge, no systematic investigation of the excited-state dynamics in bismuth sulfide has been reported hitherto.

Two are the main objectives of the present investigation: (i) to provide a quantitative assessment of the optical band gap energy versus Bi_2S_3 nanocrystal size; (ii) to reveal the basic relaxation processes of photoexcitations distinguishing the contributions of intrinsic states and traps. The synthesis conditions were systematically explored to tune size, morphology and crystallinity. High quality crystalline particles were obtained with controllable size in the range between 3 nm and 30 nm. Optical properties were investigated combining linear transmission spectroscopy with time-resolved differential transmission techniques in the 0.1 ps–1 s time range to reveal states with ultrafast and slow kinetics. For nanocrystal sizes as small as 3 nm, confinement energies are found to be much smaller than the ones found in other semiconductor nanocrystals, such as Cd and Pb sulfides and selenides. The reduced bandgap tunability of Bi_2S_3 ribbons through the control of the nanocrystal size is shown to be a general property of 1D systems, which should hold for other pnictide chalcogenides.[30] Time-resolved spectroscopy provides a wealth of novel information on the relaxation mechanisms. In agreement with the n-type character of Bi_2S_3, optically excited electrons relax down to conduction band states. Trapping of holes occurs in the sub-picosecond time scale, inhibiting radiative recombination. Shallow traps with transition energies up to 300 meV below the bandgap are observed to survive for milliseconds. The overall trap density is estimated in excess of 10^{20} cm^{-3}. The comparison of the estimated trap density with the expected density of sulphur vacancies, a well-known defect in bulk Bi_2S_3, points out to their surface origin, even in the largest investigated nanocrystals. The relationship between midgap states and surface properties is discussed in the framework of recent atomistic simulations and the charge-orbital balance model.[29,39] The efficient trapping of holes is consistent with the assumption that long oleic acid ligands are not able to passivate all trap sites in a Bi-reach nanocrystal surface, presumably due to steric effects.[41] This analysis suggests that a lower density of intragap states could be achieved by using the combination of ligands with reduced steric hindrance and different chemical affinity.[42]

2. Results and Discussion

2.1. Synthesis of Colloidal Bi_2S_3 Nanoparticles with Controlled Size

Bi_2S_3 colloidal nanoparticles were synthesized by an organometallic synthesis in the presence of oleic acid as capping agent.[2,7] Here we extensively investigate the role of different synthesis parameters, such as the injection temperature of sulfur precursor, T_i, (from 50 to 170 °C) and the reaction time (by 30 min to 6 h). Nanoparticles were purified by successive dispersion/reprecipitation and centrifugation steps in toluene/methanol and finally dispersed in anhydrous toluene. Details are reported in the Experimental Section.

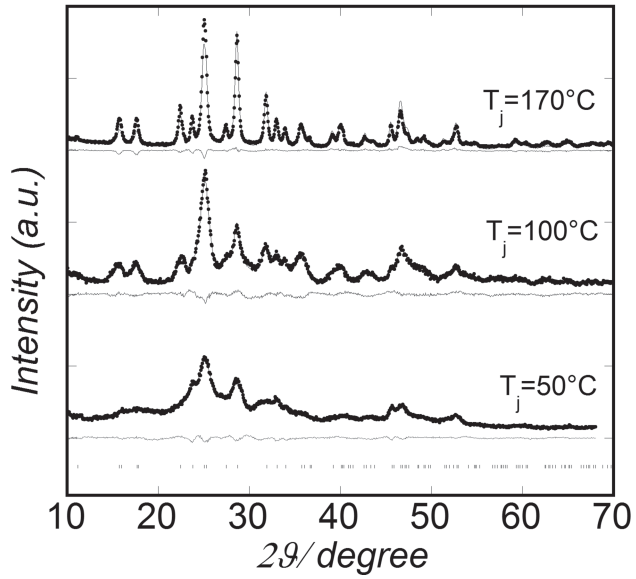

Figure 2. XRD patterns of the samples obtained at 6 h for different injection temperatures (points) with Rietveld simulations (continuous) and residuals. Crystallographic reference data (ICSD n° 30775) at the bottom

2.1.1. Structural Properties

The X-ray diffraction (XRD) patterns of the most representative samples obtained under stoichiometric conditions at 6 h with different injection temperature are reported in **Figure 2**. Full XRD data from samples obtained at different reaction times are reported in the Supporting Information. Bragg reflections indicate the presence of Bi_2S_3 with orthorhombic structure as the unique phase in all patterns. The narrowing of the peaks observed with increasing injection temperature, T_j, indicates an increase of the crystallite size. This trend is confirmed by Rietveld refinement of the XRD data. For the sample injected at T_j = 170 °C the best fit was obtained introducing a small microstrain and using a large B_j value (isotropic thermal factor) associated to structural disorder. Lattice parameters (a = 1.114, b = 1.129, c = 0.3985 nm) are in good agreement with crystallographic data (ICSD n° 30775). The fitted parameters ($<D>_{XRD}$ of the minor and major axes of nanocrystals), are reported in **Table 1** together with the final R_w (weighed pattern agreement index). In order to verify the effect of the reaction time, the refinement was also performed on the sample obtained after ½ h (Table 1, further details in the Supporting Information). The results show the formation of 9 × 26 nm anisometric single crystals (nanorods) both at 6 and ½ h,[43] indicating that the reaction time does not affect the nanocrystal size (at least under the investigated synthesis conditions).

In Table 1 (best fit in Figure 2) the evolution of the mean crystallite size with the injection temperature are also reported. The values obtained by the fit evidence that the decrease of the T_j from 170 °C to 100 °C and 50 °C are in favor of the formation of an increasing number of isotropic single crystals. However, if in the refinement procedure of the sample obtained at T_j = 100 °C a small contribution (about 8%) related to anisotropic nanocrystal is introduced, a decrease of the Rw% index by 13.8 down to a value of 8.8 is obtained, suggesting the possible presence of a low fraction of nanocrystalline rods. The reaction temperature represents therefore the key parameter in order to tune the Bi_2S_3 crystallite size.

2.1.2. Morphological Properties and Particle Size Distribution

In order to better investigate the morphology and the crystallinity of the pure bismuthinite nanoparticles, TEM bight and dark field images, and HRTEM images of the samples obtained at the different injection temperatures, together with particle size distributions calculated by Bright Field images, are reported in **Figure 3**. Information about TEM results of samples obtained at different reaction times are reported in the Supporting Information.

For all the samples, TEM images indicate that nanoparticles tend to self assemble in a monolayer on the TEM grid due to the presence of the capping agent (oleic acid) at nanoparticle surface, being the average nanoparticle distance of about 3 nm.

It is necessary to take into account that the TEM bright field images give information about particle size and morphology, but the crystalline and/or amorphous/defective nature of the nanoparticles and of nanocrystal size have to be checked by dark field mode and/or high-resolution TEM.

TEM bright and dark field images of the sample at T_j = 170 °C, reported in Figure 3a, clearly show the formation of regular rod shaped nanoparticles of average length of 25 nm (10% polydispersity) and width of 13 nm (13% polydispersity) (Table 1). The brightness of the nanorods in the dark field image is clear evidence that most of them are single crystals, being the nanorod size equal in bright and dark field mode, in good agreement with the average crystallite size values $<D>_{XRD}$ obtained by Rietveld analysis.

TEM bright field image of the sample at T_j = 100 °C (Figure 3b; Table 1) shows the presence of rod shaped particles

Table 1. Average crystallite size evaluated by Rietveld Analysis of XRD patterns with respective agreement index R_w [%]. Average particle size and polydispersity calculated by the size distributions reported in Figure 3.

Injection Temperature T_j [°C]	Reaction Time R_t [h]	Major Axis $<D>_{XRD}$ [nm]	Minor Axis $<D>_{XRD}$ [nm]	Agreement Index R_w [%]	Major Axis $<D>_{TEM}$ [nm]	σ_{TEM} [%]	Minor Axis $<D>_{TEM}$ [nm]	σ_{TEM} [%]
170	1/2	26.4(5)	9.0(5)	13.2	25	(6)	13	(10)
	6	26.1(5)	9.0(5)	8.8	25	(10)	13	(13)
100	6	–	8.7(5)	13.9	29	(14)	14	(19)
50	6	–	4.5(3)	7.5	–		3.6	

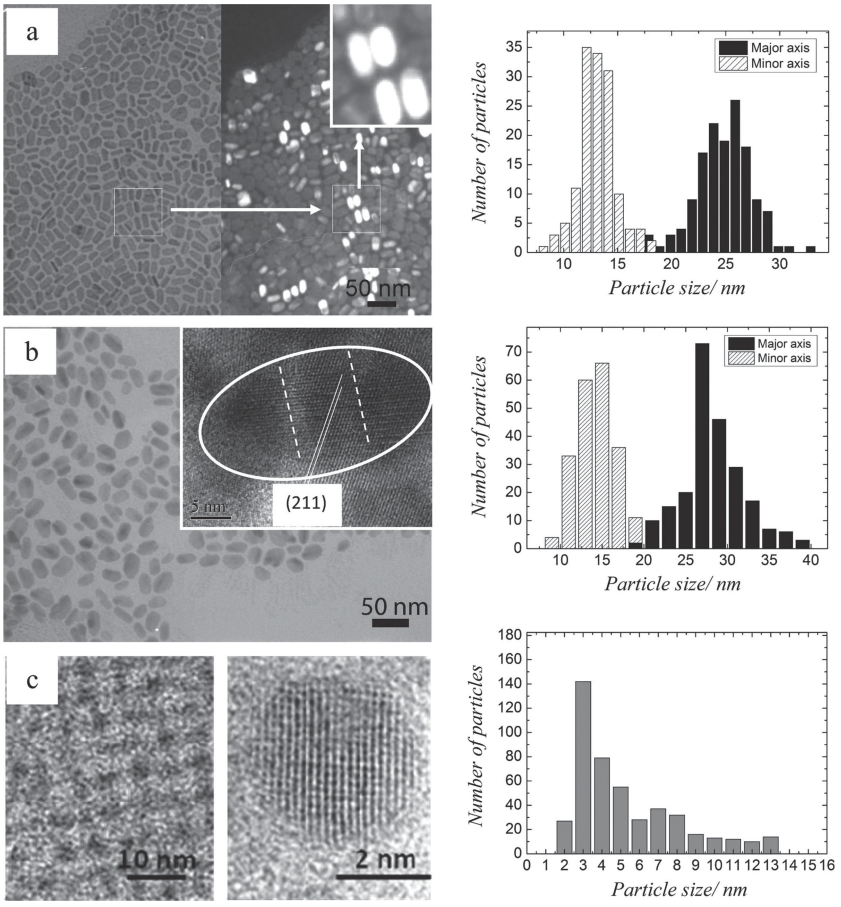

Figure 3. (a) TEM bright and dark field images of T_j = 170 °C sample. (b) Bright field image of T_j = 100 °C sample with HRTEM image (inset). (c) HRTEM images of the T_j = 50 °C sample. In the right side are reported the corresponding particle size distributions calculated by bright field images. For the T_j = 170 and 100 °C samples the size distribution of the minor and major axes of the nanorods are reported. For the T_j = 50 °C sample, the size distribution of quasi-spherical nanoparticles is characterized by a large peak at around 3 nm and a long tail extending to 13 nm.

with average sizes of 29 nm (14% polydispersity) and of 14 nm (19% polydispersity). The larger polydispersity in comparison with the sample at T_j = 170 °C is consistent with a higher spread of nanoparticle sizes for samples obtained at lower injection temperature. The average particle size values obtained by TEM are similar at the two different injection temperatures. However, for the sample at T_j = 100 °C they turn out to be three times larger in length than the average crystallite size values $<D>_{XRD}$ obtained by Rietveld analysis. This observation is confirmed by the HR-TEM image in the inset of Figure 3b which shows in fact three nanocrystals assembling to form an iso-oriented nanorod.

HRTEM images of the sample at T_j = 50 °C indicate the presence of spherical nanoparticles with a size distribution featuring a peak at around 3 nm and a long tail extending to 13 nm. (Figure 3c). The higher maximum indicates that most of them are small nanocrystals of about 3.6 nm. The average value calculated taking into account all nanoparticles (4.8 nm) is in very good agreement with the values achieved by the Rietveld refinement of XRD data (4.5 nm).

2.2. Optical and Electronic Properties

2.2.1. Energy Bandgap versus Nanocrystal Size

According to spectroscopic data on single crystals of Bi_2S_3, the room temperature absorption spectrum near the optical gap is dominated by band-to-band transitions and a broad excitonic contribution.[43] The bandgap energy, E_g, was found to be at 1.443 eV and the exciton transition at 1.413 eV. The overall absorption spectra of Bi_2S_3 nanocrystals synthesized at T_j = 50, 100, and 170 °C are reported in the inset of **Figure 4**a. To investigate the effect of the nanocrystal size on the lowest energy electronic levels in more detail, Figure 4a reports a zoom near the edge of the absorption spectra together with their first derivatives; these latter can reveal weak optical contributions and minute differences in the spectra with enhanced sensitivity. The shape of the absorbance near the optical threshold well reproduces the one reported for Bi_2S_3 single crystals, with a broad shoulder at 1.4–1.5 eV. The derivative spectrum shows that this shoulder is blue shifted by 30 meV in T_j = 50 °C nanocrystals. These spectroscopic data demonstrate that the quantum size effect is detectable but limited, despite the small dimension of the Bi_2S_3 nanocrystals. It is also worth comparing the observed shift with the confinement energies observed in nanocrystals with well-studied optical properties, such as CdSe, CdS or PbS, and PbSe. For a particle size of ~3.5 nm, the increase of the optical gap is several hundreds of meV, at least an order of magnitude higher than in Bi_2S_3.[44–47]

A theoretical quantitative assessment of the quantum confinement energies requires realistic models that take into account the atomistic nature of the nanocrystal. The size-dependence of the gap are investigated by first-principles time-dependent density functional theory by focusing on the properties of the isolated ribbon and neglecting for simplicity the effect of the weak electronic interaction due to neighboring ribbons. Undercoordinated sulfur and bismuth ions on the ribbon edges were saturated by H and OH groups, respectively. The calculated excitonic optical gap of the ribbon is reported in Figure 4b as a function of its length L. The band edge saturates at 1.5 eV for long chains. The optical gap dependence on size follows a $1/L^2$ behavior. Theoretical data show that the gap tuning becomes perceptible only for ribbon length L around 3 nm. Blue shifts larger than one hundred of meV is achieved when L is smaller than 1 nm.

A few comments are required in order to compare the experimental and theoretical values of the band gap tuning in Bi_2S_3. We note that the lengths of ribbons forming a spherical nanocrystal of diameter D must be distributed in the range $0 < L < D$: the ribbon passing through the center of the

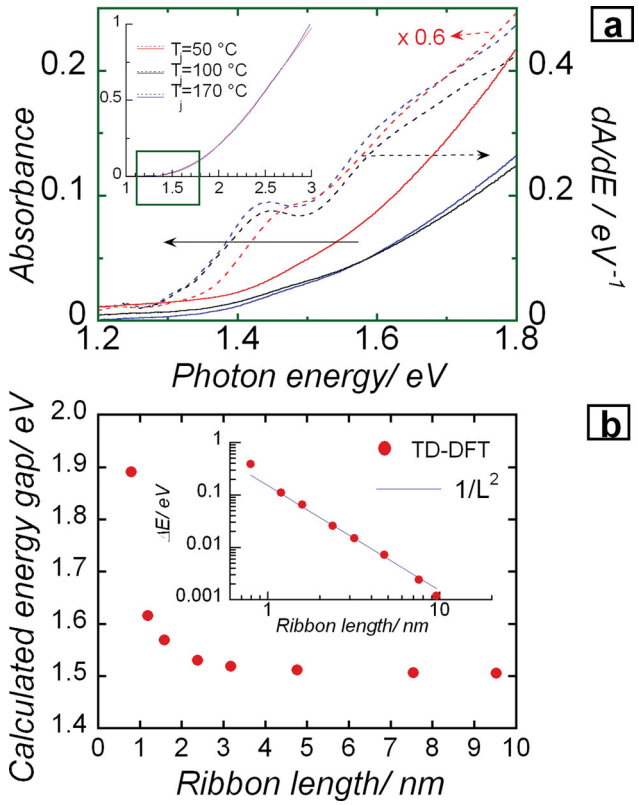

Figure 4. (a) Absorbance spectrum (continuous lines) and its first derivative (dashed lines) near the absorption edge of Bi_2S_3 nanocrystals in toluene dispersion synthesized at the injection temperatures, T_j = 50, 100, and 170 °C, respectively. The inset shows the whole UV-Vis-NIR spectra. For sake of comparison, spectra for T_j = 50, 100 °C are rescaled to the intensity of the spectrum for T_j = 170 °C. (b) Theoretical energy gap and energy gap shift (inset) of a single ribbon as a function of the ribbon length L. The lowest excitation energy was calculated through first principles methods in the framework of the time-dependent density functional formalism.

nanoparticle has a maximal length L = D while peripheral ribbons must be shorter. In other words, assuming an ensemble of spherical nanocrystals, all with the same diameter D, there exists an intrinsic distribution of ribbon lengths, as shown in the HR-TEM image of the spherical nanocrystal (T_j = 50 °C) reported in **Figure 5**. In a continuum model, the average value, $\langle L \rangle_D$, can be easily shown to satisfy the equation $\langle L \rangle_D = 2/3\ D$ (details are reported in Supporting Information). At the peak of the particle size distribution (3.5 nm), the average ribbon length is thus expected to be 2.3 nm. The expected shift of the absorption edge is calculated numerically in the continuum model from the knowledge of the dependence of the theoretical bandgap shift on L, as shown in Supporting Information. In this size range, the calculated optical shift corresponds in good approximation with that calculated for a nanoribbon of length $\langle L \rangle_D$. We find a blueshift of 30 meV, in good agreement with experiments. The possibility to achieve the challenging regime of strong confinement ($\langle L \rangle_D \sim 1$ nm, D ~ 1.5 nm) with useful energy shifts of several hundreds of meV is not, however, out of reach. According to previous experimental reports, spherical nanocrystals with diameters around 1.6 nm can be effectively synthesized by using a different synthesis approach; the observed experimental bandgap shift is consistent with the present theoretical model.[15]

In the following, we discuss the origin of the smaller Bi_2S_3 bandgap shift with respect to other semiconductor nanocrystals, such as Cd and Pb chalcopyrites, of similar size. According to basic concepts of quantum mechanics, the energy shift of the lowest confined level in an infinite potential well is expected to scale with the well size (D) and the effective mass (m_{eff}) of the excitation, following the equation $\Delta E = C\ h^2/(8m_{eff}D^2)$, where the constant C depends on the dimensionality of the confining potential. For a 1D-potential, suitable for Bi_2S_3 ribbons, C = 1, while for a 3D-spherical well, which describes the case of most nanocrystals made by II–VI and III–V semiconductors, C = 4.[48,49] This larger value accounts for the confinement energies along the three spatial dimensions (C = 3 corresponds to the case of a particle in a 3D-square well). This analysis suggests two main reasons for the comparatively small bandgap shift observed in Bi_2S_3 nanocrystals: (i) the 1D-character of the band-edge electronic states, and (ii) their heavy mass.[50,51]

2.2.2. Carrier Relaxation and Trapping on the 0.1 ps–1 ns Time Scale

Photoexcitation dynamics in Bi_2S_3 nanocrystals is monitored by using transient absorption spectroscopy.[52,53] In this nonlinear technique, a laser pulse excites the sample to trigger the basic electronic processes taking place in optoelectronic devices following photon absorption. In a simple picture, the laser pulse promotes a hot electron above the minimum of the conduction band while leaving a hole in the valence band. Both charges relax to lower energy levels and eventually recombine. Transient populations of electronic levels and the strong interactions between photoexcited electron and hole pairs produce transitory modifications in the absorption spectrum, which can be monitored by measuring the transmission of a "white" probe pulse passing through the sample at variable delays. Differential transmission spectra are defined as $\Delta T/T = (T_{on} - T_{off})/\ T_{off}$, where T_{on} (T_{off}) is the transmitted light in presence (absence) of the pump laser. $\Delta A = -\log(e)\ \Delta T/T$, where ΔA is the photoinduced variation of the nanocrystal absorbance.

Nonlinear spectra are reported in **Figure 6**a as a function of pump–probe delays for T_j = 170 °C nanocrystals. Similar nonlinear response was observed in samples grown at lower temperatures. At zero time, just after excitation, a photoinduced absorption band (PA; $\Delta T/T < 0$, $\Delta A > 0$) is observed. This contribution disappears in about 300 ps leaving room to a broad bleaching band (PB; $\Delta T/T > 0$, $\Delta A < 0$), i.e., a spectral region where the optical excitations created by the laser pulses give rise to an increase of light transmission. The PB signal monotonically grows up within the experimental detection time window of 9 ns (Figure 6b). The onset of both PA and PB occurs at the bandgap energy (arrow in Figure 6a).

Photoinduced Absorption—Carrier–Carrier Interactions: Following pump excitation, strong interactions between photoexcited electrons and holes induce a renormalization of the carrier energy levels. In bulk semiconductors, charge interaction leads to a redshift of the bandgap.[54] In absence of state-filling effects

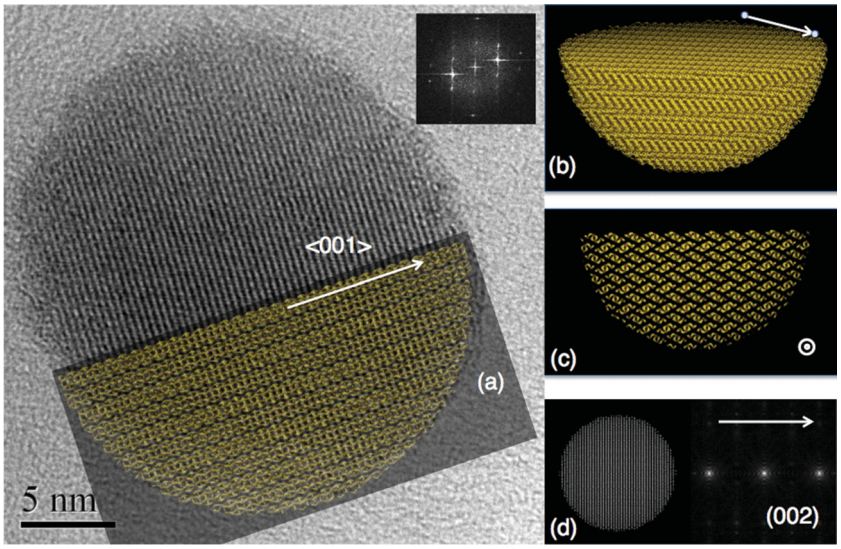

Figure 5. a) HRTEM image of a spherical nanocrystal with the superimposed ideal crystalline structure formed by ribbons aligned along the <001> direction; FFT (fast Fourier transform) of the HRTEM image in the top right corner. Perspective view (b) and cross section (c) of the atomistic crystalline structure showing the herringbone motif formed by the nanoribbons. (d) Calculated FFT (right side) of the crystal image (left side) revealing the (002) inter-plane spacing corresponding to the experimental inter-plane distance of 0.39 nm.

(t = 0), i.e. before carrier relaxation to the band edge states, the interaction-induced differential transmission spectrum, $\Delta T/T$, is thus expected to be equal to -log(e) dA/dE ΔE_r, where ΔE_r is the energy level shift. The two spectra are shown in Figure 6a. -log(e) dA/dE ΔE_r with ΔE_r = 18 meV matches very well the transient PA spectrum in the 1.3–2.2 eV spectral window, indicating that the redshift is the predominant interaction-induced effect up to 1 eV above the bandgap.

Photoinduced Bleaching—Free and Trapped Carriers: Figure 6c illustrates the mechanisms of bleaching in a simple two-band model. Photoexcited electrons and holes relax to the bottom of the conduction band and top of the valence band, respectively. Each of these thermal relaxed populations inhibits optical transitions and contributes to make the nanocrystal transparent to light near the absorption edge. The transient PB signal at E_g thus monitors the buildup of the carrier population at the band edge.

The unusually long rise time of PB observed in Bi_2S_3 nanocrystals provides evidence of a very slow energy relaxation of carriers, a process that typically occurs in the ps-time scale.[6,55] This slow process may be caused by an early relaxation of photoexcited carriers, e.g. electrons, into higher-energy conduction band minima, from which electrons eventually relax to the lowest energy minimum of the conduction band. The complex topology of the Bi_2S_3 electronic band structure corroborates this hypothesis.[50,56]

In the experiments reported in Figure 6a,b, Bi_2S_3 nanocrystals were excited by an average exciting pulse fluence of 0.17 mJ/cm^2. The photo-injected electron-hole pair density in the nanocrystals, n_{eh}, was assessed from the knowledge of the extinction coefficient per cation at the pump laser wavelength;[15] we found $n_{eh} = 1.6 \times 10^{20}$ cm^{-3}, corresponding to 0.020 excitations per Bi_2S_3 unit. The absence of any detectable photoluminescence signal, despite the fact that Bi_2S_3 is a direct semiconductor,[43] points out that only one type of carrier relaxes to the band edge states, while the other carrier is quickly trapped by intragap states. The n-type photoconductive character of Bi_2S_3 indicates that holes were captured by traps, whose average number per nanocrystal, N_t, was comparable to or larger than the number of excited holes N_h. From the amplitude of the PB signal and pulse excitation fluence, we estimate that at least 30% of photoexcited electrons was thermalized in the lowest conduction band states (details are reported in Supporting Information). In bulk Bi_2S_3, the n-type semiconducting properties of Bi_2S_3 are ascribed to the presence of sulphur vacancies. It was shown that bulk Bi_2S_3 exists with both sulphur excess and deficit.[57] For temperatures below 500 K, the upper trap density limit in the bulk results to be at least one order of magnitude smaller than the present estimate. It is therefore reasonable to conclude that the efficient hole trapping observed in Bi_2S_3 nanocrystals is mainly related to a partial passivation of surface states rather than to bulk sulphur vacancies. This deduction is supported by the observation of radiative emission in ligand-exchanged films, in which the improved surface passivation likely reduced trap density.[7]

There exists a growing experimental evidence that the surfaces of metal-chalcogenide nanocrystals are metal-rich in presence of co-ordinating ligands bound covalently to cations, regardless the use of an excess of cations during synthesis.[41,58] For off-stoichiometric surfaces, the charge-orbital balance model provides a simple method to predict whether or not traps are formed.[39] In this framework, a nanocrystal has a clean optical gap if the number of overall available valence electrons is counterbalanced by the number of available valence orbitals. Steric effects or an inappropriate coordination number of the ligand can, however, prevent the ideal charge-orbital balance to be achieved, leading to a high density of intragap states that are filled by the extra electrons supplied by unpassivated cations.[39] It is likely that this scenario also applies to Bi_2S_3 nanocrystals, in other words that nanocrystal surfaces are Bi-rich with less than two oleic acid ligands per missing S anion. The resulting energy level scheme is schematically reported in Figure 6d. The chemical potential is put close to the top of the midgap states, a choice consistent with the charge-orbital balance model, the n-type photoconducting character of Bi_2S_3 and our spectroscopic data. The high number of valence bands in Bi_2S_3 leads to the spectrally broad PB signal.[50] Under the hypothesis that each trap level can capture two holes, $N_t \sim N_h/2$, and all traps are located inside a 0.3 nm-thick shell at the nanocrystal surface, we provide a lower bound estimate of one midgap state every 16 surface Bi_2S_3 units, for a spherical nanocrystal whose size is fixed by matching the XRD nanocrystal volume (T_j = 170 °C).

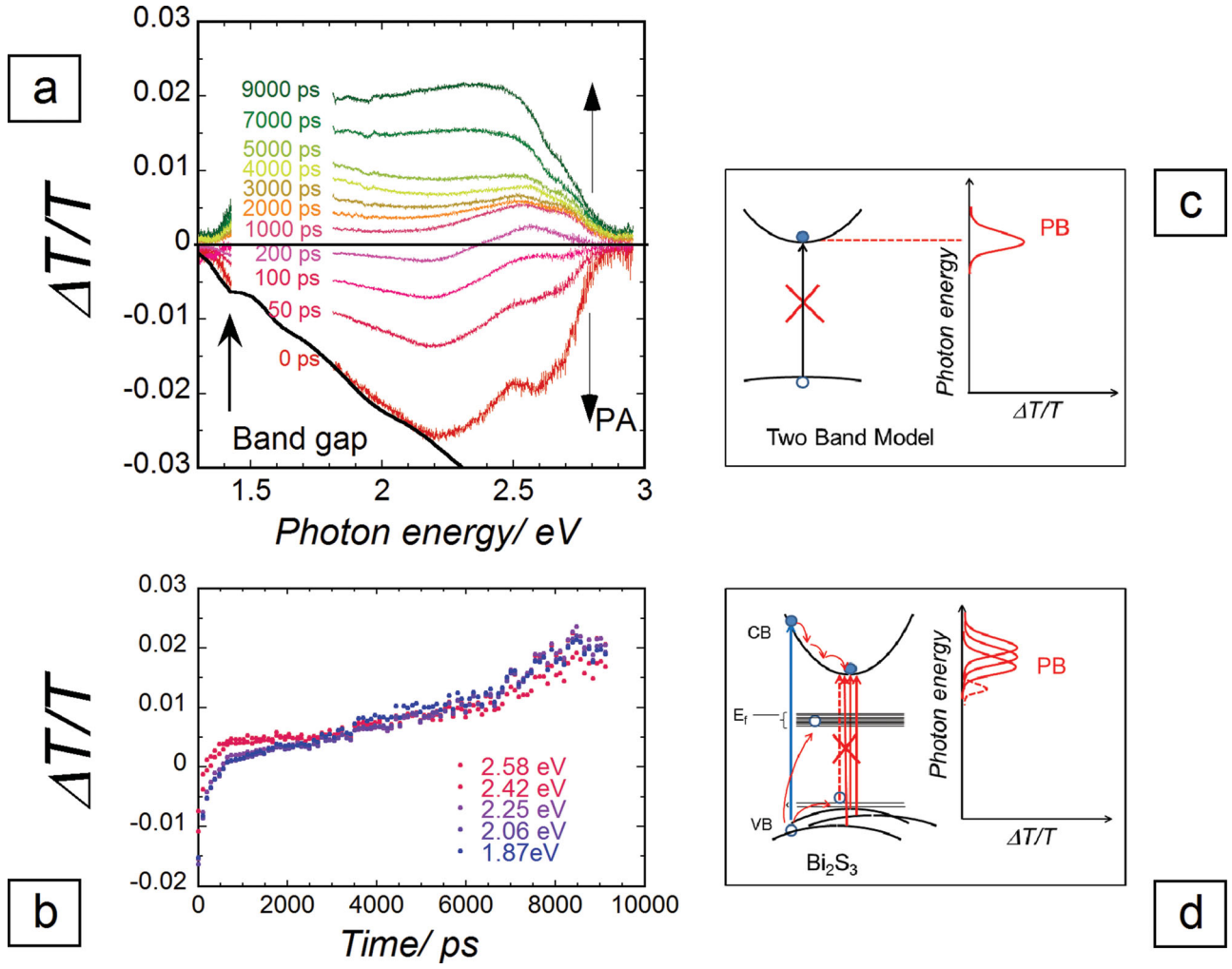

Figure 6. (a) Transient differential transmission spectra (ΔT/T) of Bi_2S_3 nanocrystals (T_j = 170 °C) in toluene dispersion as a function of the delays between the excitation ($h\nu$ = 3.16 eV) and probe laser pulses. Excitation pulse fluence: 0.17 mJ/cm^2. In the spectral range 1.4–1.8 eV, intensity instabilities of the white supercontinuum used as probe pulse do not allow measuring the transmission changes induced by the pump laser. Black curve: -log (e) dA/dE ΔE_r with ΔE_r = 18 meV. (b) Normalized transient ΔT signals at various photon energies versus pump-probe delay. (c) Graphical representation of photobleaching in a band-to-band transition model. Crossed arrow stands for suppressed optical transitions due to empty (filled) electronic levels in the valence (conduction) band. (d) Photobleaching dynamics in Bi_2S_3 nanocrystals. Intra-gap states are due to deep and shallow traps. Following photoexcitation, almost all holes are quickly trapped, while electrons relax to the bottom of the conduction band. E_f is the Fermi level, assumed close to the top of the midgap band.

2.2.3. Carrier Relaxation and Trapping on the μs-s Time Scale

Trap lifetime is typically very long, often exceeding the nanosecond time-scale by several orders of magnitude. Our measurements of differential transmission with femtosecond laser pulses are limited in range to the longest optical delay we can introduce between pump and probe pulses, which is of the order of 10 ns. **Figure 7** shows the differential transmission spectrum ΔT/T using a continuous-wave probe that bypasses the time-range limitation. In this experiment, the excitation laser are 0.4 μs-long pulses at 1 kHz repetition rate and 2.36 eV photon energy. In contrast with the linear absorption spectrum, ΔT/T reveals intense narrow structures below and just above the gap, superimposed on a continuum extending up to $h\nu$ = 2 eV. The lifetime of the nonlinear signal was determined by measuring the temporal evolution of the differential transmitted signal of the cw-probe through an oscilloscope synchronized with pump pulse train (Figure 7b). The ΔT transient reveals a short component, which follows almost rigidly the laser pulse shape, and a contribution with a much longer lifetime, comparable with the time interval between two exciting pulses (1 ms). The ΔT kinetics is independent of the transition photon energy. The narrow lines observed in the ΔT/T spectrum reveal the existence of a set of long-lived shallow traps with energy up to 300 meV below the gap, as shown in Figure 6d. The fact that these states are observed in the PB spectrum indicates that optical transitions from these states contribute to the tail absorption with a non-negligible oscillator strength. These shallow states could be associated to ligands weakly bound to energetically unfavorable nanocrystal sites. According to atomistic simulations in metal-chalcogenides, these ligand-related states can have an appreciable oscillator strength and give rise

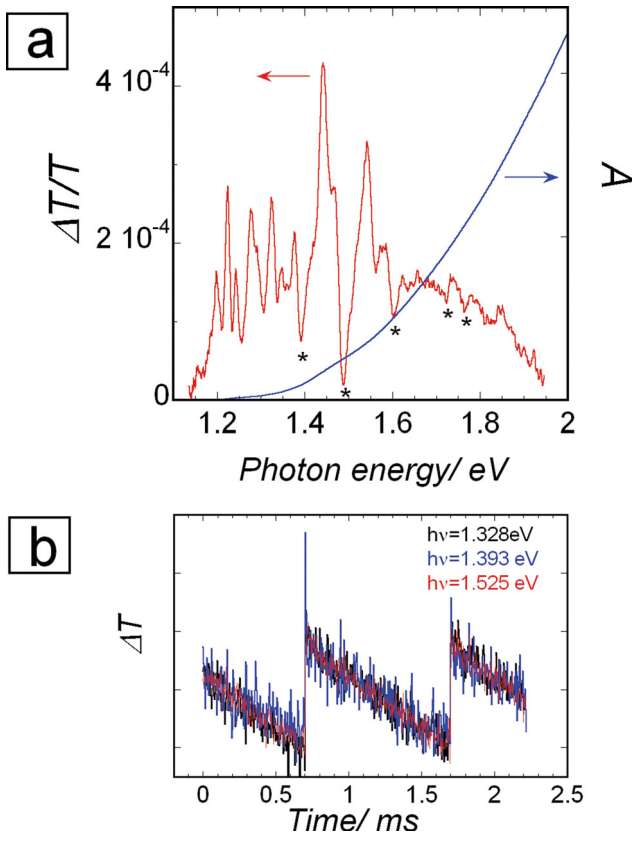

Figure 7. (a) Time-integrated differential transmission spectrum (ΔT/T) in Bi_2S_3 nanocrystals (T = 170 °C) in toluene dispersion induced by 1 kHz-pulse train ($h\nu$ = 2.33 eV). Excitation pulse fluence: 0.16 mJ/cm^2. Stars denote a Fano-like interference pattern due to a coherent mixing between narrow-line transitions involving long-lived localized states and a continuum. Blue line: linear absorption spectrum. (b) Differential transmission transients versus pump-probe delays at three different photon energies.

to intragap states near the top of the valence band.[38] PB spectrum shows an unusual pattern: near and above the band gap narrow dips are observed. This behavior can be explained in the framework of Fano's theory of optical transition lineshape: coherent mixing of a narrow resonance with a continuum can result in various asymmetric resonance shapes, ranging from a Lorentzian peak on top of a weak background (Figure 7a, photon energies below the gap), to an asymmetric s-shaped line and a spectral dip or anti-resonance behavior (Figure 7a, photon energies near and above the band gap). Narrow peaks above E_g can be explained in terms of metastable, shallow excitons resulting from lower-energy valence bands, consistently with the reported overcrowding of valence bands in Bi_2S_3.[50]

3. Conclusion

We have provided a quantitative understanding of key materials science issues concerning Bi_2S_3 nanocrystals, a non-toxic semiconductor representative of the general class of pnictide chalcogenides of the type $[Pn_4Ch_6]_n$ with considerable interest of solar energy conversion. We have addressed: (i) the bandgap tunability through the quantum size effect, (ii) the relaxation kinetics of photoexcited carries, (iii) the characteristic lifetimes, transition energies and density of trap states, and (iv) the possible origin of midgap states and their relationship with surface properties.

We have shown that the intriguing small bandgap energy dependence on the nanocrystal size stems from the one-dimensional nature of the band-edge excitations and the weak band dispersion of Bi_2S_3. To achieve useful bandgap shifts, up to 0.5 eV, the ribbon lengths should be as short as 1 nm. As nanocrystals with a fixed size are formed by the aggregation of nanoribbons of different length, an average ribbon length of 1 nm corresponds to a spherical crystal size of 1.5 nm. Although challenging, this confinement regime is effectively accessible using suitable routes to Bi_2S_3 synthesis.[15]

We have demonstrated that a large fraction of photoexcited electrons are not trapped, while all holes are quickly captured by midgap states. Energy relaxation ends up with the excitation of shallow traps with µs to ms lifetimes. The overall carrier relaxation process is consistent with the assumption of a Bi-rich nanocrystal surface in which the passivation of dangling bonds by bulky oleic acid ligands is incomplete, leading to an intragap density of states in excess of 10^{20} cm^{-3}. Recent progress in the passivation of surface states in metal–chalcogen nanocrystals suggests there exist real margins for a substantial reduction of trap density,[7] e.g., by developing a multi-ligand approach that better faces up to the complexity of nanocrystal surfaces.[42]

4. Experimental Section

Synthesis of Bi_2S_3 Colloidal Nanocrystals: An oleic acid-based organometallic synthesis is used to synthesize Bi_2S_3 colloidal nanocrystals. Bismuth(III) acetate, oleic acid and hexamethyldisilathiane are used as reactants and octadecene is employed as a solvent. Some parameters, such the injection temperature and the reaction time have been made to change. The mixture of 7.4100 g of bismuth(III) acetate (Aldrich >99%), 51 mL of oleic acid (Aldrich 90%) and 36 mL of 1-octadecene (Aldrich 90%) was heated under stirring in argon atmosphere at 90 °C for 16 h and then heated up to 170 °C.[16,58,59] A solution of 0.756 mL of HMS (Sigma Aldrich) in 30 mL of 1-octadecene was quickly injected into the flask at the same temperature (170 °C) or after cooling down at 100 °C or at 50 °C. The kinetics of the synthesis was studied sampling at controlled times. The following acronyms will be used: T_j = 170, T_j = 100 and T_j = 50 °C for samples obtained at the different injection temperatures. The samples were either cooled at room temperature or quickly transferred in a beaker containing anhydrous methanol (Panreac 99.8%) soaked in an iced bath. Purification of the nanocrystals was performed by successive dispersion/reprecipitation and centrifugation steps in toluene/methanol. Finally, the nanoparticles are dispersed in anhydrous toluene (Riedel-de-Haen). These dispersions are stable for months. The repeatability of the synthesis has been checked and other parameters have been changed such as: the amount of the solvents and the reaction atmosphere (vacuum or argon). Neither of these parameters produced significant modification of the final product.

Nanocrystal Structure and Morphology Characterization: X-ray diffraction patterns were recorded on a Seifert X3000 diffractometer with a θ–θ Bragg Brentano geometry with Cu Kα wavelength. A quantitative evaluation of nanocrystal sizes through the XRD patterns was achieved by a Rietveld refinement procedure using the MAUD software:[60] recommended fitting procedure were adopted.[61] Structural model of the identified phase of Bi2S3 were obtained by inorganic crystal structure database ICSD [Inorganic Crystal Structure Database, ICSD, 2013 Karlsruhe, Germany]. Lattice parameters, isotropic/anisotropic

average crystalline size, microstrain, preferred orientation parameter and isotropic thermal parameters were refined.[62] Weighed pattern agreement index Rw% was less than 14% for all refined patterns.

Finely ground samples were dispersed in n-octane in an ultrasonic bath and the suspension dropped on a copper grid covered with a carbon thin film for the electron microscopy observation. Micrographs and selected area electron diffraction (SAED) were obtained by a transmission electron microscope (JEOL 200CX) operating at 200 kV. High resolution images were obtained by a JEM 2010-UHR equipped with a Gatan Imaging Filter (GIF) with a 15 eV window and a 794 slow scan CCD camera.

Linear Optical Absorption: UV-Visible absorption spectra were recorded with a Perkin Elmer Lambda 950 spectrophotometer. All spectra were recorded on toluene-based suspensions.

Transient Differential Transmission Spectroscopy: The laser source employed for these experiments was a Ti:Sapphire regenerative amplifier (Quantronix Integra C) operating at a repetition rate of 1 kHz and emitting at 786 nm in wavelength. The white-light continuum 150 fs-long laser pulses, generated by focusing the output of the regenerative amplifier, attenuated to approximately 1 μJ energy per pulse, on a 1 mm sapphire plate were used a probe pulses. The white-light continuum pulses had a variable delay with respect to pump pulses (394 nm wavelength, 150 fs-long). Pump and probe beams were focused on a 1 mm quartz cuvette filled with nanocrystals dispersed in toluene. The cumulative effect of spectral chirp and wavefront distortion of laser pulses resulted in a 200-fs time-delay resolution. Optical spectra were recorded with a CCD camera (Andor Newton. 16 bit resolution, used in vertical binning) coupled to a grating spectrometer (Acton SP2300i, equipped with a grating 300 groves/mm). Differential transmission $\Delta T/T = (T_{on}- T_{off})/T_{off}$ was obtained by recording sequential transmission spectra with (T_{on}) and without (T_{off}) pump pulses illuminating the sample.

cw-Differential Transmission Spectroscopy: The exciting source was the second harmonic of a Nd:YLF laser (B.M.I., 600) operating at a repetition rate of 1 kHz and emitting 0.4 μs-long pulses ($h\nu = 2.36$ eV). The cw-emission of a xenon lamp was used as a probe light source. Differential transmission ΔT was detected by a look-in amplifier (SRS, SR830 DSP) triggered by the output of the pump laser. The lifetime of the nonlinear signal was determined by measuring the temporal evolution of the differential transmitted signal of the cw-probe through an oscilloscope (Tektronix, TDS 3054 B) synchronized with the pump pulse train.

Computational Methodologies: The calculations where performed with the TURBOMOLE package [TURBOMOLE V6.4 2012, a development of University of Karlsruhe and Forschungszentrum Karlsruhe GmbH, 1989–2007, TURBOMOLE GmbH, since 2007; available from http://www.turbomole.com] which uses a frequency–space implementation of TDDFT.[63] In this implementation, based on the linear response of the density–matrix, the poles of the linear response function correspond to vertical excitation energies and the pole strengths to the corresponding oscillator strengths.[64] In particular, we computed the first 10 electronic transitions. We adopted the B3LYP hybrid functional and a basis set formed by Gaussian-type Orbitals.[65] In particular, we used the default Split-Valence Polarized basis set for both Bi and S. Effective core potentials were also employed to properly describe the core electrons of bismuth.

Supporting Information

Supporting Information is available from the Wiley Online Library or from the author.

Acknowledgements

This work has been funded by Regione Autonoma della Sardegna under L. R. 7/2007 CRP3_114 "Design di nanomateriali ibridi organici/inorganici per l'energia fotovoltaica" and CRP-249078 "Nanomateriali eco-compatibili per celle fotovoltaiche a stato solido di nuova generazione", by the Italian Institute of Technology under Project Seed "POLYPHEMO" (grant n° B21J0000290007), by (MIUR Under PON 2007–2013 (Project NETERGIT), and by Consiglio Nazionale delle Ricerche (Progetto Premialità RADIUS). We acknowledge computational support by IIT Platform "Computation" and by CINECA through ISCRA Initiative (Project OPTO-BIS).

Received: November 16, 2013
Revised: December 17, 2013
Published online: February 20, 2014

[1] Y. Shirasaki, G. J. Supran, M. G. Bawendi, V. Bulović, *Nat. Photonics* **2013**, *7*, 13.
[2] J. P. Clifford, G. Konstantatos, K. W. Johnston, S. Hoogland, L. Levina, E. H. Sargent, *Nat. Nanotechnol.* **2009**, *4*, 40.
[3] E. H. Sargent, *Nat. Photonics* **2012**, *6*, 133.
[4] I. Gur, N. A. Fromer, M. L. Geier, A. P. Alivisatos, *Science* **2005**, *310*, 462.
[5] Semiconductor Nanocrystal Quantum Dots: Synthesis, Assembly, Spectroscopy and Applications, 1st Ed. (Ed:A. Rogach), Springer, Berlin **2010**.
[6] Nanocrystal Quantum Dots, 2nd Ed. (Ed: V. I. Klimov), CRC Press, Taylor & Francis Group, Boca Raton **2010**, p. 2010.
[7] A. K. Rath, M. Bernechea, L. Martinez, F. P. G. de Arquer, J. Osmond, G. Konstantatos, *Nat. Photonics* **2012**, *6*, 529.
[8] Z. Wang, S. Qu, X. Zeng, J. Liu, F. Tan, L. Jin, Z. Wang, *Appl. Surf. Sci.* **2010**, *257*, 423.
[9] L. Martinez, A. Stavrinadis, S. Higuchi, S. L. Diedenhofen, M. Bernechea, K. Tajima, G. Konstantatos, *Phys. Chem. Chem. Phys.* **2013**, *15*, 5482.
[10] Q. Guo, H. W. Hillhouse, R. Agrawal, *J. Am. Chem. Soc.* **2009**, *131*, 11672.
[11] J. Puthussery, S. Seefeld, N. Berry, M. Gibbs, M. Law, *J. Am. Chem. Soc.* **2011**, *133*, 716.
[12] Y. Wu, C. Wadia, W. Ma, B. Sadtler, A. P. Alivisatos, *Nano Lett.* **2008**, *8*, 2551.
[13] C. Wadia, A. P. Alivisatos, D. M. Kammen, *Environ. Sci. Technol.* **2009**, *43*, 2072.
[14] J. Tang, A. P. Alivisatos, *Nano Lett.* **2006**, *6*, 2701.
[15] L. Cademartiri, R. Malakooti, P. G. O'Brien, A. Migliori, S. Petrov, N. P. Kherani, G. A. Ozin, *Angew. Chem. Int. Ed. Engl.* **2008**, *47*, 3814.
[16] G. Konstantatos, L. Levina, J. Tang, E. H. Sargent, *Nano Lett.* **2008**, *8*, 4002.
[17] H.-C. Liao, M.-C. Wu, M.-H. Jao, C.-M. Chuang, Y.-F. Chen, W.-F. Su, *CrystEngComm* **2012**, *14*, 3645.
[18] C. E. Patrick, F. Giustino, *Adv. Funct. Mater.* **2011**, *21*, 4663.
[19] G. Xiao, Q. Dong, Y. Wang, Y. Sui, J. Ning, Z. Liu, W. Tian, B. Liu, G. Zou, B. Zou, *RSC Adv.* **2012**, *2*, 234.
[20] L. Shi, D. Gu, W. Li, L. Han, H. Wei, B. Tu, R. Che, *J. Alloys Compd.* **2011**, *509*, 9382.
[21] A. Maria Ibanez, Pablo Guardia, Alexey Shavel, Doris Cadavid, Jordi Arbiol, Joan Ramon Morante, A. Cabot, *J. Phys. Chem. C* **2011**, 7947.
[22] J. S. Owen, J. Park, P.-E. Trudeau, A. P. Alivisatos, *J. Am. Chem. Soc.* **2008**, *130*, 12279.
[23] S. Shen, Y. Zhang, L. Peng, B. Xu, Y. Du, M. Deng, H. Xu, Q. Wang, *CrystEngComm* **2011**, *13*, 4572.
[24] R. Malakooti, L. Cademartiri, Y. Akçakir, S. Petrov, A. Migliori, G. A. Ozin, *Adv. Mater.* **2006**, *18*, 2189.
[25] D. J. Riley, J. P. Waggett, K. G. U. Wijayantha, *J. Mater. Chem.* **2004**, *14*, 704.
[26] M. Graetzel, R. A. J. Janssen, D. B. Mitzi, E. H. Sargent, *Nature* **2012**, *488*, 304.

[27] I. J. Kramer, L. Levina, R. Debnath, D. Zhitomirsky, E. H. Sargent, *Nano Lett.* **2011**, *11*, 3701.
[28] J. Tang, H. Liu, D. Zhitomirsky, S. Hoogland, X. Wang, M. Furukawa, L. Levina, E. H. Sargent, *Nano Lett.* **2012**, *12*, 4889.
[29] V. Calzia, G. Malloci, G. Bongiovanni, A. Mattoni, *J. Phys. Chem. C* **2013**, DOI: 10.1021/jp405740b.
[30] R. Caracas, X. Gonze, *Phys. Chem. Miner.* **2005**, *32*, 295.
[31] I. J. Kramer, E. H. Sargent, *ACS Nano* **2011**, *5*, 8506.
[32] E. H. Sargent, *IEEE J. Sel. Top. Quantum Electron.* **2008**, *14*, 1223.
[33] P. Nagpal, V. I. Klimov, *Nat. Commun.* **2011**, *2*, 486.
[34] M. Saba, M. Aresti, F. Quochi, M. Marceddu, M. A. Loi, J. Huang, D. V Talapin, A. Mura, G. Bongiovanni, *ACS Nano* **2013**, *7*, 229.
[35] P. Stadler, B. R. Sutherland, Y. Ren, Z. Ning, A. Simchi, S. M. Thon, S. Hoogland, E. H. Sargent, *ACS Nano* **2013**, 0.
[36] P. Kambhampati, *Acc. Chem. Res.* **2011**, *44*, 1.
[37] J. I. Saari, E. A. Dias, D. Reifsnyder, M. M. Krause, B. R. Walsh, C. B. Murray, P. Kambhampati, *J. Phys. Chem. B* **2013**, *117*, 4412.
[38] O. Voznyy, *J. Phys. Chem. C* **2011**, *115*, 15927.
[39] O. Voznyy, D. Zhitomirsky, P. Stadler, Z. Ning, S. Hoogland, E. H. Sargent, *ACS Nano* **2012**, *6*, 8448.
[40] R. Suarez, P. K. Nair, P. V Kamat, *Langmuir* **1998**, *7463*, 3236.
[41] W. Ma, J. M. Luther, H. Zheng, Y. Wu, A. P. Alivisatos, *Nano Lett.* **2009**, *9*, 1699.
[42] A. H. Ip, S. M. Thon, S. Hoogland, O. Voznyy, D. Zhitomirsky, R. Debnath, L. Levina, L. R. Rollny, G. H. Carey, A. Fischer, K. W. Kemp, I. J. Kramer, Z. Ning, A. J. Labelle, K. W. Chou, A. Amassian, E. H. Sargent, *Nat. Nanotechnol.* **2012**, *7*, 577.
[43] A. Cantarero, A., Martinez-Pastor, J., Segura, A., Chevy, *Appl. Phys. A* **1988**, *45*, 125.
[44] C. B. Murray, D. J. Noms, M. G. Bawendi, *J. Am. Chem. Soc.* **1993**, *115*, 8706.
[45] Y. Wang, A. Suna, W. Mahler, R. Kasowski, *J. Chem. Phys.* **1987**, *87*, 7315.
[46] A. Lipovskii, E. Kolobkova, V. Petrikov, I. Kang, A. Olkhovets, T. Krauss, M. Thomas, J. Silcox, F. Wise, Q. Shen, S. Kycia, *Appl. Phys. Lett.* **1997**, *71*, 3406.
[47] G. Pellegrini, G. Mattei, P. Mazzoldi, *J. Appl. Phys.* **2005**, *97*, 073706.
[48] L. E. Brus, *J. Chem. Phys.* **1984**, *80*, 4403.
[49] A. L. Efros, A. L. Efros, *Sov. Phys. Semicond.* **1982**, *16*, 772.
[50] P. Larson, V. Greanya, W. Tonjes, R. Liu, S. Mahanti, C. Olson, *Phys. Rev. B* **2002**, *65*, 085108.
[51] M. R. Filip, C. E. Patrick, F. Giustino, *Phys. Rev. B* **2013**, *87*, 205125.
[52] M. Saba, S. Minniberger, F. Quochi, J. Roither, M. Marceddu, A. Gocalinska, M. V. Kovalenko, D. V. Talapin, W. Heiss, A. Mura, G. Bongiovanni, *Adv. Mater.* **2009**, *21*, 4942.
[53] M. Marceddu, M. Saba, F. Quochi, A. Lai, J. Huang, D. V Talapin, A. Mura, G. Bongiovanni, *Nanotechnology* **2012**, *23*, 015201.
[54] G. Bongiovanni, J. L. Staehli, *Phys. Rev. B* **1989**, *39*, 8359.
[55] S. L. Sewall, R. R. Cooney, K. E. H. Anderson, E. A. Dias, D. M. Sagar, P. Kambhampati, *J. Chem. Phys.* **2008**, *129*, 084701.
[56] A deeper analysis of this relaxation phenomenon would deserve more specific optical measurements. This is, however, outside the aim of the present investigation.
[57] H. Rau, *J. Phys. Chem. Solids* **1981**, *42*, 257.
[58] D. Zhitomirsky, M. Furukawa, J. Tang, P. Stadler, S. Hoogland, O. Voznyy, H. Liu, E. H. Sargent, *Adv. Mater.* **2012**, *24*, 6181.
[59] A. K. Rath, M. Bernechea, L. Martinez, F. P. G. de Arquer, J. Osmond, G. Konstantatos, *Nat. Photonics* **2012**, *6*, 529.
[60] L. Lutterotti, S. Matthiers, H.-R. Wenk *JUCr News* **1999**, *21*, a4.
[61] R. Delhez, T. H. de Keijser, J. I. Langford, D. Lour, E. J. Mittemeijer, E. J. Sonneveld, The Rietveld Method (Ed: R. A. Young), Oxford University Press, Oxford UK **1993**; pp.132–166.
[62] W. A. Dollase, *J. Appl. Cryst.* **1986**, 267.
[63] R. Bauernschmitt, R. Ahlrichs, *Chem. Phys. Lett.* **1996**, *256*, 454.
[64] M. E. Casida, Recent Advances in Density Functional Theory (Ed: D. P. Chong), Vol. *I.*, World Scientific, Singapore **1995**.
[65] A. D. Becke, *J. Chem. Phys.* **1993**, *98*, 5648.